CATALYSIS

Thermal catalytic reforming for hydrogen production with zero CO_2 emission

Mi Peng[1]†, Yuzhen Ge[1]†, Rui Gao[2]†, Jie Yang[3]†, Aowen Li[4]†, Zhiheng Xie[1], Qiaolin Yu[1], Jie Zhang[1], Hiroyuki Asakura[5], Hui Zhang[6], Zhi Liu[7], Qi Zhang[8], Jin Deng[3], Jihan Zhou[1]*, Wu Zhou[4]*, Graham J. Hutchings[9]*, Ding Ma[1]*

Carbon-neutral hydrogen production is of key importance for the chemical industry of the future. We demonstrate a new thermal catalytic route for the partial reforming of ethanol into hydrogen and acetic acid with near-zero carbon dioxide emissions. This reaction is enabled by a catalyst containing a high density of atomic Pt_1 and Ir_1 species supported on a reactive alpha-molybdenum carbide substrate, achieving a hydrogen production rate of 331.3 millimoles of hydrogen per gram catalyst per hour and an acetic acid selectivity of 84.5% at 270°C, and is therefore more energy-efficient compared with standard reforming. Techno-economic analysis of partial ethanol reforming demonstrates the potential profitability for operation at an industrial scale, presenting the opportunity to produce hydrogen and acetic acid with a substantially reduced carbon dioxide footprint.

The reforming of fossil fuels is currently the predominant route for industrial hydrogen (H_2) production (1, 2), but it is associated with considerable CO_2 emissions (3). Greener alternatives such as water electrolysis (4) and biomass gasification (5) could reduce the carbon footprint of H_2 production, but these face bottlenecks in efficiency, cost-effectiveness, and scalability. Partial oxidation ($C_2H_5OH + 1.5O_2 = 2CO_2 + 3H_2$) and full steam reforming ($C_2H_5OH + 3H_2O = 2CO_2 + 6H_2$) ($6$, 7) of ethanol have also been actively explored for possible carbon-neutral H_2 production, especially using bio-derived renewable ethanol. Although these processes show some advantages over conventional H_2 production routes (Fig. 1A) (8), partial oxidation is intrinsically limited by the stoichiometrically low H_2 production rate (9), whereas the highly endothermic nature of full steam reforming (Fig. 1B) (10, 11) requires high operating temperatures that promote undesired side reactions (12). Notably, both pathways convert 100%
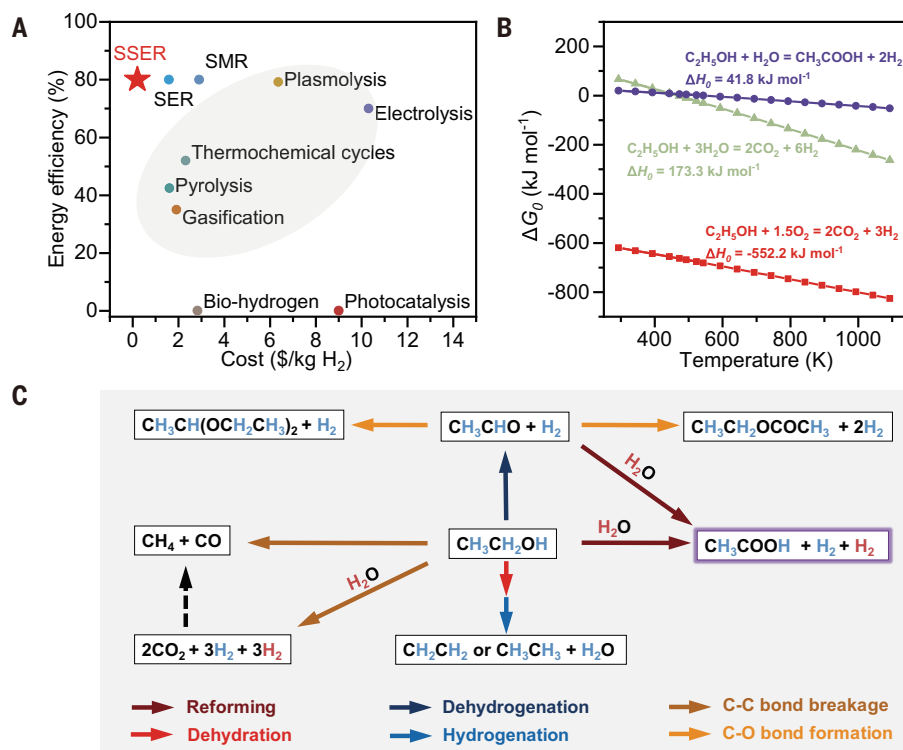
[1]Beijing National Laboratory for Molecular Science, New Cornerstone Science Laboratory, College of Chemistry and Molecular Engineering, Peking University, Beijing, China. [2]School of Chemistry and Chemical Engineering, Inner Mongolia University, Hohhot, China. [3]CAS Key Laboratory of Urban Pollutant Conversion, Anhui Province Key Laboratory of Biomass Clean Energy, Department of Applied Chemistry, University of Science and Technology of China, Hefei, China. [4]School of Physical Sciences, University of Chinese Academy of Sciences, Beijing, China. [5]Department of Applied Chemistry, Faculty of Science and Engineering, Kindai University, Osaka, Japan. [6]Shanghai Synchrotron Radiation Facility, Shanghai Advanced Research Institute, Chinese Academy of Sciences, Shanghai, China. [7]Center for Transformative Science, Shanghai Tech University, Shanghai, China. [8]SINOPEC Shanghai Research Institute of Petrochemical Technology Co., Ltd., Shanghai, China. [9]Max Planck-Cardiff Centre on the Fundamentals of Heterogeneous Catalysis, FUNCAT, Cardiff Catalysis Institute, School of Chemistry, Cardiff University, Cardiff, UK.
*Corresponding author. Email: dma@pku.edu.cn (D.M.); wuzhou@ucas.ac.cn (W.Z.); jhzhou@pku.edu.cn (J.Z.); hutch@cardiff.ac.uk (G.J.H)
†These authors contributed equally to this work.

of the carbon atoms into CO_2, depleting the carbon resources.

Reaction pathway and catalyst design

A comprehensive exploration of the ethanol reforming process revealed a complex reaction network (Fig. 1C). An ideal H_2 production pathway from ethanol reforming should both be thermodynamically favorable and minimize net carbon emission (13). We propose selective partial reforming of ethanol with water to form acetic acid and H_2 ($C_2H_5OH + H_2O = CH_3COOH + 2H_2$) as the more valuable route (rust red in Fig. 1C). It offers multiple benefits: (i) the reforming process extracts H_2 from both ethanol and water, producing more H_2 than the dehydrogenation process from a stoichiometric perspective; (ii) carbon atoms remain in the liquid phase, generating a valuable chemical product and minimizing CO_2 emissions; (iii) the co-produced acetic acid fulfills rising global demand and serves as a critical intermediate for the production of additional chemicals, including cellulose acetate, vinyl acetate monomer, and polyvinyl acetate (14). By contrast, conventional catalysts for ethanol reforming, including noble metal catalysts (such as Pt and Pd) and non-noble metal catalysts (such as, Ni, Cu, and Co) (15–21), tend to convert the carbon atoms in ethanol into CO_x, leading to a net carbon-positive process with CO_x emission (without taking into account the origin of ethanol).

Designing a new catalyst that enables the reforming reaction while preventing C-C bond breakage (22) is crucial for selectively facilitating this partial reforming route into acetic acid. We developed a highly dispersed Pt/Ir metal catalyst supported on alpha-molybdenum carbide (α-MoC) that efficiently promoted the partial steam reforming of ethanol into H_2 and acetic acid under temperatures considerably lower than that required in conventional ethanol steam reforming. We selected α-MoC as a reactive support to construct the interfacial catalysts in view of its unprecedented capability of activating water at low temperatures (23, 24) and its strong interactions with noble metals, which created a high density of interfacial active sites for methanol reforming (25, 26).

Compared with methanol reforming, ethanol reforming is thermodynamically less favored (27, 28) and requires a higher density of reforming sites to facilitate the reaction. More importantly, to achieve a high selectivity toward acetic acid, the cleavage of the C-C bond in the ethanol backbone, which leads to the formation of undesired C_1 products such as CO, CO_2, or CH_4, (see Fig. 1C) must be suppressed. Because C-C bond cleavage typically requires a di-σ carbon-metal configuration, large metal catalytic ensembles that contain abundant metal-metal bonds must be eliminated (29). Previous studies on Ir/α-MoC and Pt/α-MoC catalysts revealed that Ir has a stronger interaction with α-MoC (26, 30, 31), which leads to much higher dispersion than Pt under the same metal loading, although the intrinsic dehydrogenation activity of Ir is lower than that of Pt (26, 32). We expected co-loading of Ir and Pt onto α-MoC improve Pt dispersion, thereby constructing a catalyst (M/α-MoC, M = Pt/Ir) with a high density of atomic interfacial sites (i.e., active interfaces formed by atomic-scale Pt or Ir species, including Pt or Ir single atoms as well as fully exposed clusters (33), over the reactive α-MoC support) that are beneficial for the efficient and selective reforming of ethanol into acetic acid.

Catalyst synthesis and characterization

We synthesized a series of Pt/Ir-based catalysts supported on α-MoC using the incipient wetness impregnation method (see methods for details; the number before Pt or Ir denotes the weight percentage of the metal loading). X-ray diffraction (XRD) revealed the formation of Pt particles (2θ = 39.8°) in 3Pt/α-MoC, and the diffraction for crystalline Pt became more pronounced in 6Pt/α-MoC (Fig. 2A and fig. S1). By contrast, Ir particles were not detected even at a metal loading of 6 weight percent (wt%) (Fig. 2A and fig. S2). Importantly, with the addition of Ir, 3Pt3Ir/α-MoC did not show obvious XRD peaks for either Pt or Ir crystals at a total metal loading of 6 wt%, confirming that Ir indeed enhanced the dispersion of Pt species. Loading the Pt and Ir species with equal concentration onto an inert SiO_2 support (3Pt3Ir/SiO_2) produced metal particles that were resolved by XRD (Fig. 2A). This 3Pt3Ir/ SiO_2 catalyst served as a reference catalyst containing abundant large metal ensemble sites.

The metal dispersions were further analyzed using extended x-ray absorption fine-structure (EXAFS). For the 1Pt/α-MoC catalyst, the Pt-Pt

Fig. 1. Survey of H$_2$ production routes. (**A**) Comparison of energy efficiency and costs of various H$_2$ production routes. Detailed references listed in table S1. SMR, steam methanol reforming; SER, steam ethanol reforming; SSER, selective steam ethanol reforming. (**B**) Thermodynamic evaluation of different ethanol conversion routes. (**C**) Schematics of the reaction network for ethanol reforming: (i) ethanol is converted into acetaldehyde through dehydrogenation and forms the corresponding (hemi)acetal through condensation, with the latter not contributing to net H$_2$ production; (ii) ethanol goes through dehydration/hydrogenation to form ethylene and ethane, neither generating H$_2$; (iii) ethanol can produce CO$_2$ and CO/CH$_4$ through C-C bond breakage, a side reaction consuming H$_2$; (iv) ethanol goes through full reforming with water and produces H$_2$ and CO$_2$. Although this process produces the most H$_2$, it requires higher temperatures and does not preserve the carbon resource at all. (v) Ethanol selectively reforms with water to produce H$_2$ from both reactants while preserving high-value C$_2$ products such as acetic acid.

coordination number (CN) was 1.0, indicating the formation of small Pt clusters even at a low Pt loading. The average CN$_{Pt-Pt}$ increased with higher Pt loading, reaching 4.9 for 6Pt/α-MoC (Fig. 2B, figs. S3 to S8, and tables S2 and S3), suggesting the formation of a substantial number of Pt ensemble sites. By contrast, no Ir-Ir coordination was detected in the 1Ir/α-MoC and 3Ir/α-MoC catalysts, and the average CN$_{Ir-Ir}$ for 6Ir/α-MoC was only 1.9, indicating a much higher dispersion of Ir on α-MoC compared with Pt (Fig. 2B). At a total metal loading of 6 wt%, the 3Pt3Ir/α-MoC catalyst showed no Ir-Ir scattering and a CN$_{Pt-Pt}$ of 2.3, suggesting atomic dispersion of Ir species and enhanced dispersion of Pt compared with 3Pt/α-MoC.

We used atomic number (Z) contrast imaging and electron energy-loss spectroscopy (EELS) mapping on aberration-corrected scanning transmission electron microscopy (STEM) to visualize the atomic-scale structures of the 3Pt/α-MoC and 3Pt3Ir/α-MoC catalysts. For 3Pt/α-MoC, STEM Z-contrast image combined with EELS mapping revealed the coexistence of atomically dispersed Pt species and Pt clusters with a diameter of ~1 nm (Fig. 2, C and D, and fig. S9 and S10). For 3Pt3Ir/α-MoC, the Z-contrast imaging could not differentiate Pt and Ir (fig. S10), but the EELS mapping in Fig. 2F, in combination with the Z-contrast image in Fig. 2E, revealed the coexistence of atomically dispersed Pt and Ir species, as well as small Pt clusters on the α-MoC support. The Pt and Ir EELS signals extracted from Fig. 2F were highly confined to single pixels, demonstrating that the elemental-sensitive EELS mapping has single-atom sensitivity (34). In addition, comparison of Fig. 2D and Fig. 2F revealed a much-improved dispersion of Pt species in 3Pt3Ir/α-MoC than that in 3Pt/α-MoC, consistent with the conclusion drawn from XAS.

Atomic electron tomography (AET) (35, 36) was used to investigate the three-dimensional (3D) distribution and coordination of Pt (and Ir) atoms in metal clusters in the 3Pt/α-MoC and 3Pt3Ir/α-MoC catalysts (see methods and

figs. S11 to S13). Although sampling is limited with AET, it still provides valuable insights into the 3D distribution of the Pt(Ir) species on the α-MoC support, and the local metal-metal CNs calculated from the reconstructed atomic coordinates can be informative. In 3Pt/α-MoC, for a 1495-atom motif containing 48 Pt atoms, most Pt atoms had CN$_{Pt-Pt}$ ranging from 3 to 9 (Fig. 2G and movie S1). By contrast, in the 3Pt3Ir/α-MoC catalyst, most of the Pt/Ir atoms were present as single atoms distributed at point defect sites on α-MoC, with only a small portion of Pt/Ir atoms showing a CN between 1 and 5 (Fig. 2H and movie S2). These comprehensive structural analysis results consistently demonstrate that Ir species promoted the dispersion of Pt species on α-MoC to create a high density of interfacial active sites.

Catalytic evaluation

In situ spectroscopy experiments were performed to examine the potential of the 3Pt3Ir/α-MoC catalyst for activating water and ethanol by tracking the adsorption and evolution of surface species. The O 1s x-ray photoelectron spectroscopy (XPS) under ultrahigh vacuum showed two peaks at 530.3 and 531.6 eV that we attributed to residual oxygen and hydroxyl groups, respectively, on the surface of α-MoC (Fig. 3A and fig. S14) (31). After dosing water onto the catalyst at room temperature (RT) in near-ambient-pressure XPS (NAP-XPS) experiments, an adsorbed water peak at 533.2 eV (37) emerged, accompanied by an increase in the hydroxyl group peak (531.6 eV). This observation suggests that water dissociates into hydroxyl species over 3Pt3Ir/α-MoC at RT, consistent with previous reports on other α-MoC based catalysts (38).

In addition, dosing ethanol onto the 3Pt3Ir/α-MoC catalyst at RT caused increases in the two peaks at 531.8 eV and 533.2 eV, attributed to adsorbed oxygenates and ethanol (39), respectively (Fig. 3B and fig. S14), indicating the dissociative adsorption of ethanol. As the temperature increased, the peak assigned to adsorbed oxygenates increased, indicating enhanced activation of ethanol, despite the Pt and Ir species remaining unchanged during this process (figs. S15 and S16). Meanwhile for 3Pt3Ir/SiO$_2$, feeding water and ethanol does not lead to dissociation at RT (fig. S17). The dissociation of ethanol over the 3Pt3Ir/α-MoC catalysts was further confirmed by transient kinetic analysis (figs. S18 and 19). When C$_2$H$_5$OD was fed to the pretreated 3Pt3Ir/α-MoC surface at RT, both H$_2$ and hydrogen deuteride were detected in the outlet gas, suggesting that the catalyst could dissociate both C-H and O-H bonds of ethanol at RT.

To assess the feasibility of ethanol-water partial reforming over these catalysts, we used in situ Fourier-transforming infrared (FTIR) spectroscopy (Fig. 3C) to monitor the adsorption (evident by the presence of C-H stretching
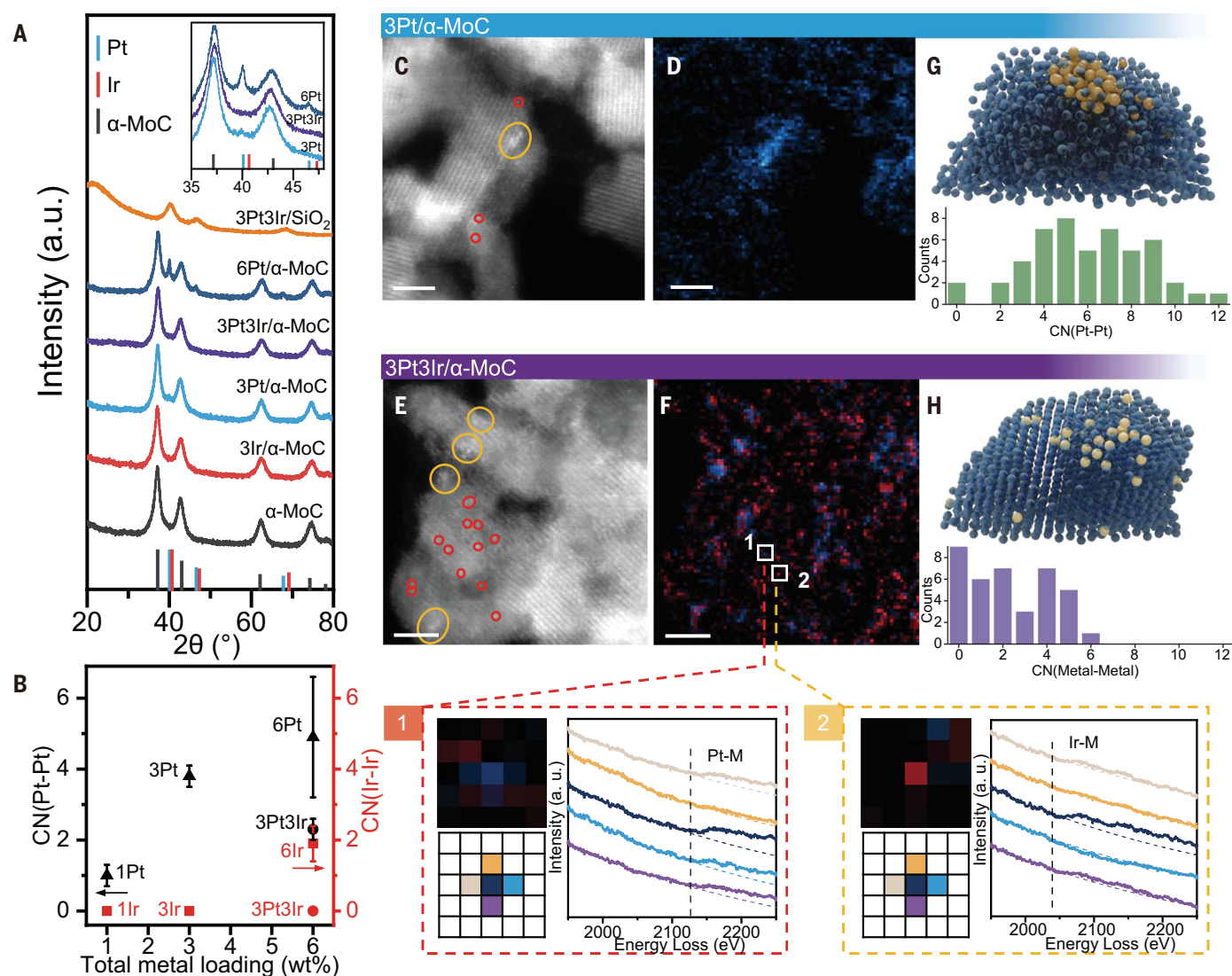
Fig. 2. Structural characterization of the PtIr/α-MoC catalysts. (**A**) XRD profiles of α-MoC supported Pt/Ir catalysts with different metal loadings. Inset notes the enlarged region of the Pt(111) diffraction peak. (**B**) Coordination numbers (CN) of Pt-Pt and Ir-Ir in different catalysts obtained from EXAFS fitting. Triangles indicate Pt/α-MoC; squares, Ir/α-MoC; circles, PtIr/α-MoC. (**C**) and (**D**) High-angle annular dark-field (HAADF) image (C) and the corresponding EELS mapping (D) of 3Pt/α-MoC. (**E**) and (**F**) HAADF image (E), and the corresponding EELS mapping (F) of 3Pt3Ir/α-MoC. Metal clusters and atomically dispersed species are marked with yellow and red circles, respectively. Pt is presented in blue and Ir in red in the EELS mapping. The bottom panels present the enlarged Pt/Ir elemental maps and the corresponding pixel indexes of the areas marked by the white squares 1 and 2 in (F) and the EELS spectra extracted from the pixels with the corresponding colors. (**G**) and (**H**) The metal atom distribution in 3Pt/α-MoC (G) and 3Pt3Ir/α-MoC (H) is obtained through 3D reconstruction from tomographic tilt series. The blue spheres show Mo atoms and the golden spheres represent Pt/Ir atoms. The bar charts show the M-M (M = Pt or Ir) coordination number distribution calculated from the reconstructed 3D structural model. Scale bars in (C) to (F) are 2 nm.

in ethanol at 2981 cm^{-1}), the effective dehydrogenation of ethanol (evident by the increase of C=O stretching at 1758 cm^{-1}, C-O bending mode at 1377 cm^{-1}, and C-O stretching mode at 1242 cm^{-1} in acetaldehyde) (40) and the overall reactivity (formation of acetic acid) among α-MoC, 3Pt3Ir/α-MoC, and 3Pt3Ir/SiO$_2$ catalysts. For the 3Pt3Ir/SiO$_2$ catalyst containing large metal ensembles, the peaks associated with carbon monoxide (C-O stretching at 2063 cm^{-1}) and methane (C-H stretching at 3016 cm^{-1}, degenerate bending mode at

1303 cm^{-1}) were clearly resolved (Fig. 3C, i) once the vapor of ethanol/water mixture was introduced over the catalyst. This result indicated that large ensembles of noble metals were highly active for C-C bond cleavage (41), making them unfavorable for partial ethanol reforming.

By contrast, ethanol dehydrogenation was particularly effective on α-MoC (Fig. 3C, ii), as evidenced by the appearance of bands associated with acetaldehyde at 1242 cm^{-1} and 1758 cm^{-1} after the introduction of the ethanol/water vapor mixture onto the catalyst at 270°C.

Although C-C bond breakage was not observed, we were unable to resolve the peak associated with CH$_3$COO- over α-MoC, possibly because of its inability to further transform acetaldehyde into the corresponding acid. Notably, only on the 3Pt3Ir/α-MoC catalyst containing abundant atomic-scale interfaces between Pt$_1$ or Ir$_1$ and α-MoC, could the asymmetric stretching mode of O=C-O- in CH$_3$COO- at 1612 cm^{-1} (42) be resolved, even from the early stages of reforming (Fig. 3C, iii). Thus, these interfaces were critical for the formation of acetic acid.
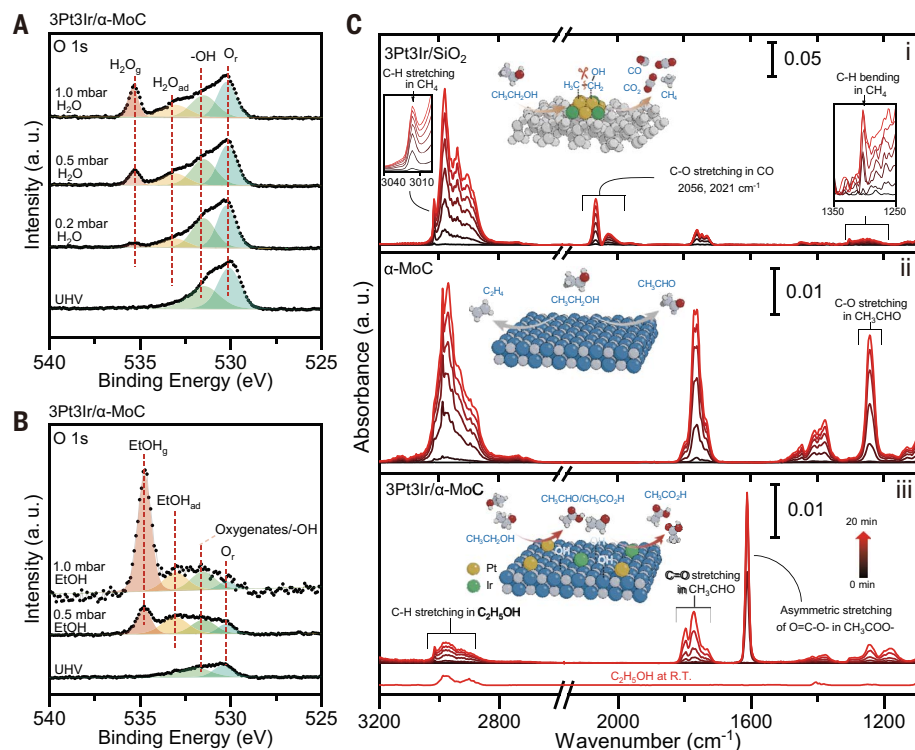
Fig. 3. Reaction network and site requirement studies for partial reforming of ethanol. (**A**) and (**B**) NAP-XPS results of the 3Pt3Ir/α-MoC catalyst under different pressure of H_2O (A) and ethanol (B). The samples were treated in the corresponding environments noted in the figure for 30 min before measuring. O_r represents residual oxygen; H_2O_g and H_2O_{ad} denote water in the gas phase and water adsorbed on the catalyst surface, respectively; $EtOH_g$ and $EtOH_{ad}$ refer to ethanol in the gas phase and ethanol adsorbed on the catalyst surface, respectively. (**C**) In situ FTIR spectra of water and ethanol adsorption over (i) 3Pt3Ir/SiO$_2$, (ii) α-MoC, and (iii) 3Pt3Ir/α-MoC catalysts at 270°C. The fresh catalysts after pretreatment were followed by Ar flushing for 30 min at 270°C, and then exposed to ethanol and water atmosphere. Inset includes schematic illustration of possible dominant reaction pathways on each catalyst.

These results demonstrated that the surface of 3Pt3Ir/α-MoC could readily activate both water and ethanol in the initial stage of the reaction, following the pathway shown in Fig. 3C, indicating potentially excellent catalytic performance in steady-state reactions. The pristine α-MoC sites favored the dehydrogenation of ethanol into acetaldehyde and the dissociation of H_2O into hydroxyls (*31*, *43*), whereas the interfaces between atomic-scale Pt or Ir species and α-MoC were pivotal for the partial reforming of ethanol with water. Importantly, eliminating the formation of Pt(Ir)-Pt(Ir) ensembles was crucial for preventing C-C bond cleavage and for the low selectivity toward CO_x and methane in the reaction.

We evaluated the selective reforming performance using a continuous-flow fixed-bed reactor (the mass balance, calculated based on the number of carbon atoms, ranged from 101 to 109% for all catalysts, see methods for details). Ethanol reforming typically follows a dehydrogenation-reforming sequential pathway (*44*), so the performance of acetaldehyde reforming with water was evaluated first on α-MoC-based catalysts (Fig. 4A). Pure α-MoC

shows negligible activity toward acetaldehyde reforming, which is in good agreement with the in-situ FTIR results. By contrast, with the loading of Pt or Ir, the activity increased substantially, suggesting that noble metals or metal/carbide interfaces played a vital role in the reforming process. Although 3Pt/α-MoC showed a higher H_2 production rate than 3Ir/α-MoC, its selectivity toward undesired C_1 products was much higher (~38 versus ~8%), primarily because of its tendency to aggregate under high metal loadings that promoted C-C bond cleavage. The co-loading of Pt and Ir boosted activity toward H_2 production and high selectivity, exceeding 80%, toward acetic acid. These results supported our proposal that a high density of Pt_1 and Ir_1 single atoms on molybdenum carbide would facilitate H_2 production through reforming while suppressing C-C cleavage.

We then evaluated ethanol reforming with water on these catalysts. Pure α-MoC showed a H_2 production rate of 51.3 mmol$_{H_2}$/(g$_{cat}$·h) at 543 K, with acetaldehyde as the main product (selectivity ~53.0%) (Fig. 4B and table S4) and ethylene/ethane accounting for ~20% se-

lectivity. Loading either Pt or Ir onto α-MoC substantially increased the H_2 generation rate (figs. S20 and S21). A comparison of the reforming activity of Pt/α-MoC and Ir/α-MoC at a low metal loading of 1% (fig. S22) revealed higher intrinsic ethanol reforming activity for Pt/α-MoC and the essential role of atomic-scale noble-metal/carbide interface in reforming, similar to what we observed for acetaldehyde reforming. For comparison, supporting atomically dispersed Pt species on an inert carbon support yielded neglectable reforming activity, highlighting the essential role of the Pt(or Ir)/α-MoC interface. At a higher metal loading of 3%, both 3Pt/α-MoC and 3Ir/α-MoC demonstrated superior H_2 generation activity 147.3 mmol$_{H_2}$/(g$_{cat}$·h) and 176.0 mmol$_{H_2}$/(g$_{cat}$·h), respectively) and a high acetic acid selectivity exceeding 50%. Further increasing the individual metal loading to 6% did not improve the activity or selectivity toward acetic acid (figs. S20 and S21).

Notably, with co-loading of Pt and Ir, 3Pt3Ir/α-MoC exhibited the highest efficiency, achieving a H_2 generation rate of 331.3 mmol$_{H_2}$/(g$_{cat}$·h) after optimizing reaction condition (figs S23 and 24), and surpassed previously reported results in thermocatalysis, photocatalysis, and electrocatalysis (Fig. 4D and tables S5 and S6). A high water-to-ethanol ratio was used (9:1) under the optimal condition, which is critical for both thermodynamic and kinetic reasons, as detailed in the theoretical investigation section below. Additionally, 3Pt3Ir/α-MoC demonstrated a high selectivity of 84.5% toward acetic acid, with less than 10% toward C_1 products (CO, CO$_2$, and CH$_4$), showing better performance than fully reforming processes under similar reaction temperatures (Fig. 4D and table S7). The presence of a high density of interfacial M_1/α-MoC (M_1 = Pt_1 or Ir_1) sites effectively blocked the undesired reaction routes, such as the formation of acetaldehyde and other byproducts.

A durability test on the 3Pt3Ir/α-MoC catalyst demonstrated promising stability in both activity and selectivity over a 100-hour run (Fig. 4C). The activity for H_2 production decreased by 21% from its initial level within the first 100 hours of reaction, but the rate of decline gradually slowed as testing proceeded. Over this period, the catalyst achieved a cumulative H_2 production of 27.3 mol per gram of catalyst, accompanied by the generation of 19.2 mol of acetic acid. Furthermore, XRD characterization revealed no obvious structural change of the catalyst after usage (fig. S25), suggesting a potentially much longer life span.

Theoretical investigation

To better understand the enhanced catalytic performance of the 3Pt3Ir/α-MoC catalyst, we performed density functional theory (DFT) calculations to explore the ethanol reforming paths and reaction mechanisms (Fig. 5 and
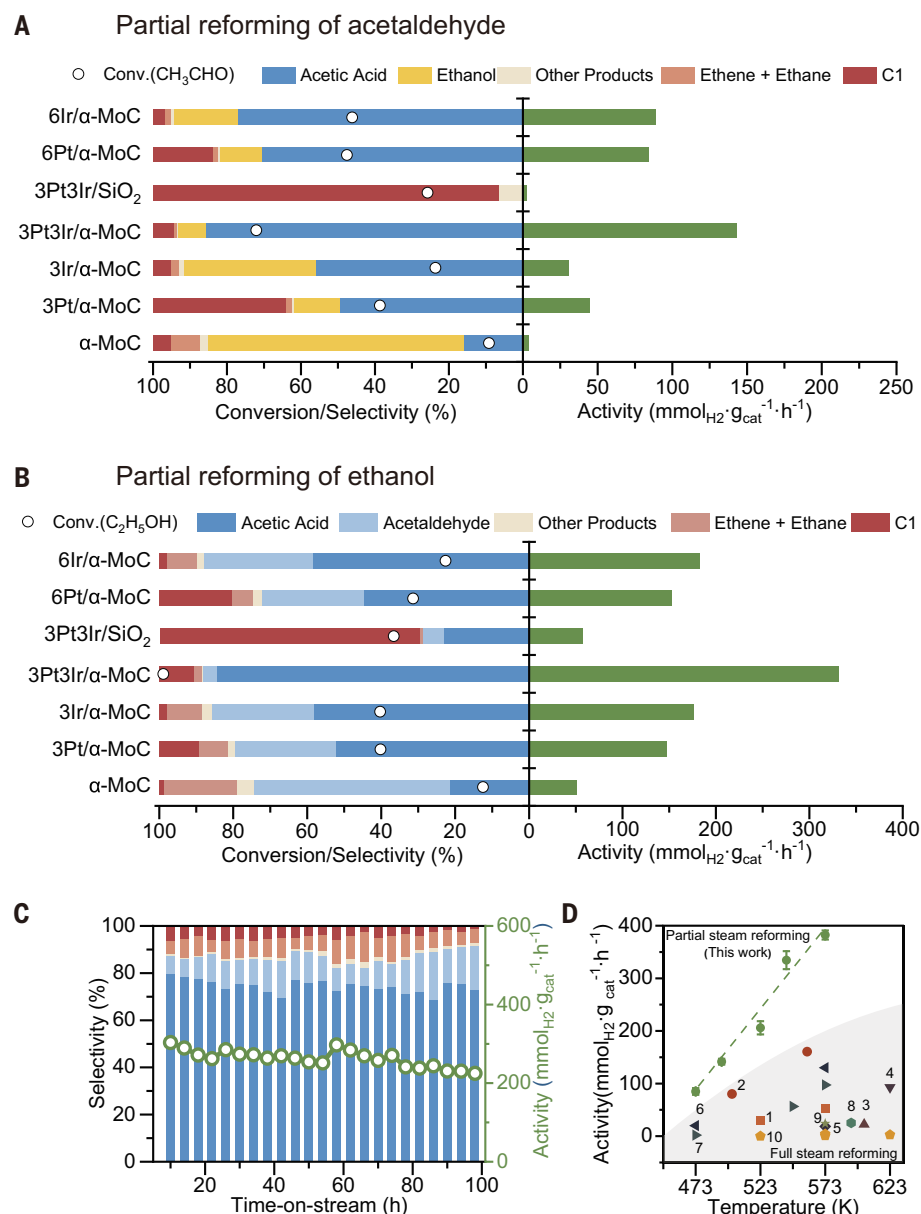
Fig. 4. Catalytic performance for partial reforming of ethanol. (**A**) Catalytic performance of supported Pt/Ir catalysts for partial reforming of acetaldehyde. Reaction conditions: 543 K, weight-hourly space velocity (WHSV) of acetaldehyde = 10.6 $g_{acetaldehyde}/(g_{cat} \cdot h)$, flow rate of the carrier gas (5% Ar in N_2) = 60 mL/min, n (acetaldehyde): n (H_2O) = 1: 9. (**B**) Catalytic performance of supported Pt/Ir catalysts for partial reforming of ethanol. Reaction conditions: 543 K, $WHSV_{ethanol}$ = 10.6 $g_{ethanol}/(g_{cat} \cdot h)$, flow rate of the carrier gas (5% Ar in N_2) = 60 mL/min, n (ethanol): n (H_2O) = 1: 9. (**C**) Long-term stability test of 3Pt3Ir/α-MoC for partial reforming of ethanol with water. The reaction condition is the same as in (B). (**D**) Comparison of H_2 production activity through ethanol steam reforming in literature and in this work. The same symbol indicates data from the same reference (detailed references are listed in table S7).

figs. S26 to S37). With inputs from structural characterizations, we constructed five structural models to represent different catalytic sites: Mo-terminated α-MoC(111) as pristine α-MoC; Pt(111) and Pt(210) representing the flat surface sites and step sites of Pt clusters/particles, respectively; Pt_1/MoC(111) and Ir_1/MoC(111) for atomically dispersed Pt and Ir on α-MoC, respectively.

We first explored the reaction pathways of ethanol decomposition on the α-MoC(111) surface. Figure 5A and fig. S26 show that on α-MoC(111) the terminal C-H bond of ethanol first dissociated into surface *CH_2CH_2OH and then went through two favored routes. One involved the dissociation of C-O bond to form ethylene with an effective energy barrier of 0.80 eV, and the other generated the most

thermodynamically stable intermediate CH_2CO with an effective energy barrier of 0.78 eV. However, subsequent transformation of this intermediate into acetaldehyde and acetic acid required a much higher energy barrier (>1.3 eV), suggesting that ethanol reforming would be hindered on α-MoC by the accumulation of C_2 species. However, this result did not fully align with the high acetaldehyde selectivity we observed in our experiment (Fig. 4B), signaling the strong influence from surface hydroxyls.

Note that under our experimental conditions, a high surface hydroxyl coverage was expected during the reaction because of the high feedstock ratio of water to ethanol (9:1) and the high activity of α-MoC for water dissociation (*31*). To unveil the interaction between carbon intermediates and hydroxyls, we performed calculations of CH_2CH_2OH dissociation on the α-MoC(111) surface with low and high hydroxyl coverages of 1/3 ML and 5/9 ML, respectively (fig. S27). The rate-determining steps of ethanol decomposition under 5/9 ML hydroxyl coverage are presented in Fig. 5D. A comparison of Fig. 5A and Fig. 5D revealed that the overall energy barrier toward the formation of acetaldehyde was lowered to 0.92 eV at higher hydroxyl coverage, whereas the barrier toward ethylene formation increased to 1.10 eV. This result suggested that ethylene formation could be to some extent inhibited by the increased hydroxyl coverage from water dissociation on α-MoC, consistent with the experimental selectivity.

For comparison, the pathways of ethanol decomposition on Pt particles were also investigated (Fig. 5B and fig. S28). The results showed that the reforming process on the Pt(111) flat surface did not exhibit a specific preference for any single product, as the calculated energy barriers toward acetaldehyde, acetic acid, CH_2CO intermediate, and C_1 products were similar. However, on the Pt(210) step surface, the energy barrier for C-C bond breakage of the most stable CH_2CO intermediate was reduced to 0.81 eV (Fig. 5C and fig. S29), suggesting that Pt particles, containing rich step surfaces, favored the formation of C_1 products. This result aligned well with the experimental findings on catalysts containing large metal ensembles, such as the 3Pt3Ir/SiO_2, 3Pt/α-MoC, and 6Pt/α-MoC (Fig. 4B, fig. S20, and table S4).

To investigate the catalytic effects of atomic M_1/α-MoC (M_1 = Pt_1 or Ir_1) interfacial sites, we calculated the pathways for the reaction of CH_2CO (the most stable C_2 intermediate on α-MoC, Fig. 5A) into acetic acid and acetaldehyde on Pt_1/MoC(111) and Ir_1/MoC(111) at high hydroxyl coverage (Fig. 5, E and F, and fig. S30,). The energy barriers toward the formation of acetic acid were reduced to 0.58 eV on Pt_1/MoC(111) and 0.73 eV on Ir_1/MoC(111), substantially lower than those on pristine
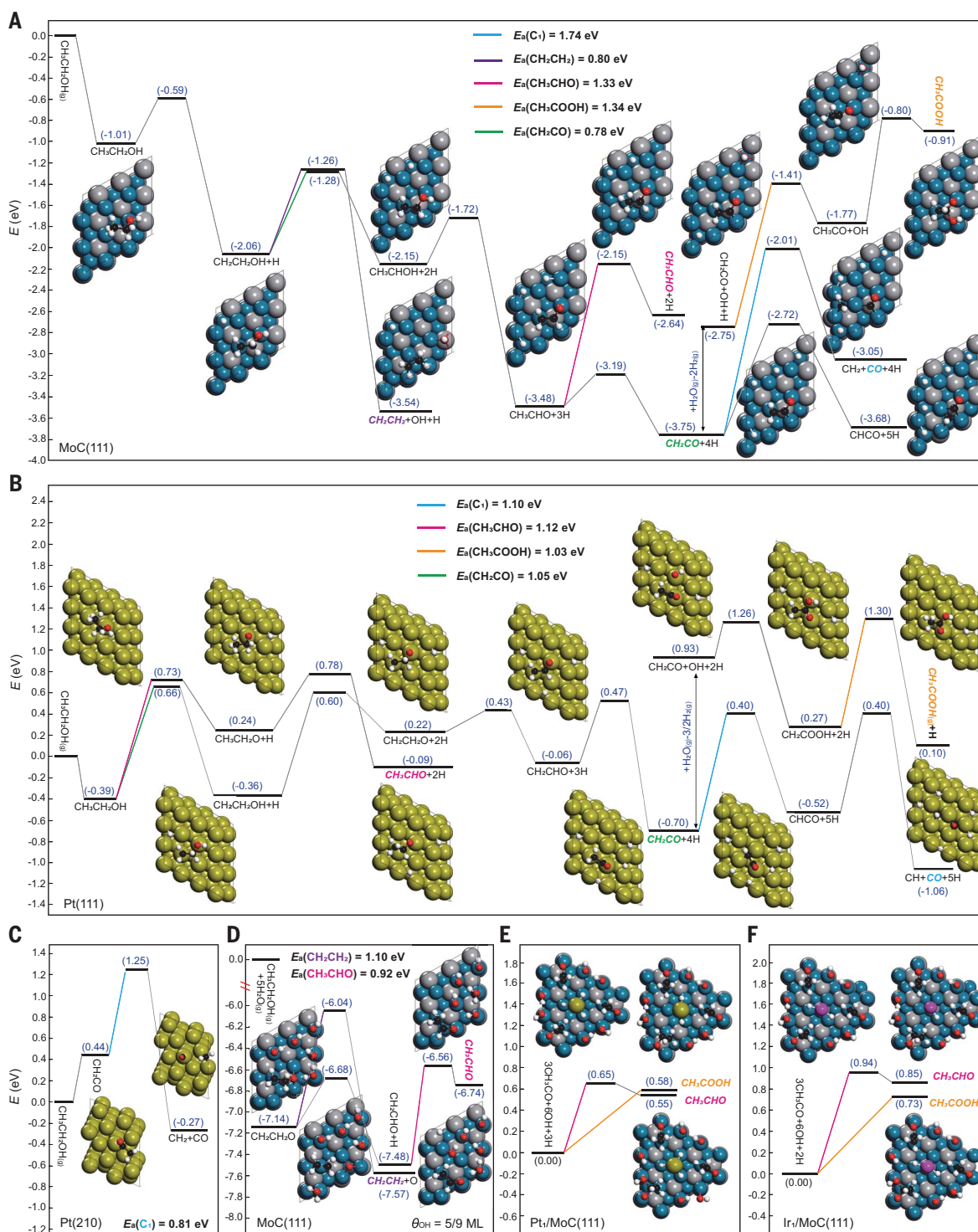
Fig. 5. Reaction pathways of ethanol reforming on PtIr/α-MoC catalysts.
(**A**) Energy profiles for ethanol conversion pathways on the pure α-MoC (111) surface. (**B**) Energy profiles for ethanol conversion pathways on the flat Pt(111) surface. (**C**) Energy profile for the conversion pathway of the most stable intermediate CH$_2$CO on the Pt(210) step surface. (**D**) Energy profiles for the corresponding formation pathways of C$_2$H$_4$ and CH$_3$CHO on the α-MoC(111) surface with a hydroxyl coverage of 5/9 ML. (**E**) and (**F**) The energy profiles for the rate-determining steps of CH$_3$CHO and CH$_3$COOH formation from the most stable intermediate CH$_2$CO and hydroxyl on the Pt$_1$/MoC(111) (E) and Ir$_1$/MoC (111) (F) interfaces (CH$_2$CO/OH = 1:2, their total coverage = 9/16 ML). The Pt, Ir, Mo, C, O, and H atoms are shown in gold, pink, dark cyan, gray, red, and white, respectively; C atoms from ethanol are marked in black.

α-MoC and metallic Pt surfaces. Thus, the interfacial structure formed by atomically dispersed Pt (or Ir) and α-MoC facilitated the selective generation of acetic acid, aligning well with experimental observations, highlighting the importance of a high density of interfacial M$_1$/α-MoC sites in turning the reaction pathway toward partial reforming into acetic acid. Our calculations also suggest that small fully

exposed metal clusters on MoC exhibit structural and adsorption characteristics (figs. S31 to S37 and movies S3 and S4) akin to those of Pt_1/MoC or Ir_1/MoC sites, thus also contribute to the overall catalytic activity. However, when large Pt or Ir particles form on α-MoC surface, C-C bond cleavage is considerably facilitated, leading to the formation of undesired products like CO_2 and CH_4.

Techno-economic analysis

Having demonstrated the outstanding catalytic performance of 3Pt3Ir/α-MoC in selective partial ethanol reforming, we further conducted an exhaustive techno-economic analysis and life cycle assessment to evaluate its prospect in an industry-scale plant for the production of H_2 and acetic acid (fig. S31, analysis detailed shown in tables S8 to S11). The evaluation indicates that the reforming plant can potentially achieve an attractive return on sales (ROS) ratio (table S12), surpassing the average ROS of the chemical industry (45) and demonstrating the economic viability of this process. Moreover, over the life span of the catalyst, carbon emissions for the production of H_2, and acetic acid are reduced by 21.9 and 38.6%, respectively, compared with conventional routes (fig. S32, analysis details shown in table S13). The decrease in fossil energy consumption is even more significant, with reductions of 51 and 86%, respectively. These results provide robust support for the sustainable attributes and feasibility of scaling up this process. Note that this process is still in its primary stage, more research and development efforts are required to further improve its efficiency and adaptability (see table S12 and associated discussions).

Outlook

In summary, we report a new thermal catalytic process for the selective partial reforming of ethanol with water to produce H_2 and acetic acid, which preserves the carbon resources in a high-valued liquid product and substantially cuts net carbon emissions. A rational design and construction of a high density of atomic $M_1/α$-MoC interfacial sites while avoiding the formation of large metal ensembles is demonstrated to be crucial for tuning the reforming pathway toward a high selectivity of acetic acid and for achieving an unprecedented H_2 generation activity of 331.3 $mmol_{H2}/(g_{cat}·h)$ at low temperatures. This process could be scalable and profitable at an industrial scale, offering a promising avenue for sustainable green H_2 production with zero CO_2 emissions.

REFERENCES AND NOTES

1. G. Chen, X. Tu, G. Homm, A. Weidenkaff, *Nat. Rev. Mater.* **7**, 333–334 (2022).
2. E. Lewis *et al.*, "Comparison of commercial, state-of-the-art, fossil-based hydrogen production technologies" (National Energy Technology Laboratory, report DOE/NETL-2022/3241, 2022).
3. International Energy Agency (IEA), "The Future of Hydrogen" (IEA, 2019).
4. A. J. Shih *et al.*, *Nat. Rev. Methods Primers* **2**, 84 (2022).
5. H. de Lasa, E. Salaices, J. Mazumder, R. Lucky, *Chem. Rev.* **111**, 5404–5433 (2011).
6. G. A. Deluga, J. R. Salge, L. D. Schmidt, X. E. Verykios, *Science* **303**, 993–997 (2004).
7. L. V. Mattos, G. Jacobs, B. H. Davis, F. B. Noronha, *Chem. Rev.* **112**, 4094–4123 (2012).
8. A. Palanisamy, N. Soundarrajan, G. Ramasamy, *Environ. Sci. Pollut. Res. Int.* **28**, 63690–63705 (2021).
9. W. J. Wang, Y. Q. Wang, *Int. J. Hydrogen Energy* **33**, 5035–5044 (2008).
10. D. Pashchenko, *Int. J. Hydrogen Energy* **44**, 30865–30875 (2019).
11. M. Nielsen *et al.*, *Nature* **495**, 85–89 (2013).
12. S. Ogo, Y. Sekine, *Fuel Process. Technol.* **199**, 106238 (2020).
13. E. Balaraman, E. Khaskin, G. Leitus, D. Milstein, *Nat. Chem.* **5**, 122–125 (2013).
14. A. C. Dimian, A. A. Kiss, *Chem. Eng. Res. Des.* **159**, 1–12 (2020).
15. A. L. M. da Silva *et al.*, *J. Catal.* **318**, 67–74 (2014).
16. A. L. M. da Silva *et al.*, *Catal. Today* **164**, 262–267 (2011).
17. A. H. Braga *et al.*, *ACS Catal.* **11**, 2047–2061 (2021).
18. M. Martinelli *et al.*, *Appl. Catal. A Gen.* **610**, 117947 (2021).
19. M. Kourtelesis *et al.*, *Appl. Catal. B* **284**, 119757 (2021).
20. H. Meng *et al.*, *Nat. Commun.* **14**, 3189 (2023).
21. W. Shi *et al.*, *Adv. Energy Mater.* **13**, 2301920 (2023).
22. M. H. Haider *et al.*, *Nat. Chem.* **7**, 1028–1032 (2015).
23. Y. Deng *et al.*, *Acc. Chem. Res.* **52**, 3372–3383 (2019).
24. Y. Ge *et al.*, *J. Am. Chem. Soc.* **143**, 628–633 (2021).
25. L. Lin *et al.*, *J. Am. Chem. Soc.* **143**, 309–317 (2021).
26. L. Lin *et al.*, *Nature* **544**, 80–83 (2017).
27. M. Compagnoni, A. Tripodi, I. Rossetti, *Appl. Catal. B* **203**, 899–909 (2017).
28. S. M. de Lima *et al.*, *J. Catal.* **268**, 268–281 (2009).
29. P. S. Kirlin, B. C. Gates, *Nature* **325**, 38–40 (1987).
30. S. Li *et al.*, *Natl. Sci. Rev.* **9**, nwab026 (2021).
31. X. Zhang *et al.*, *Nature* **589**, 396–401 (2021).
32. L. Sun *et al.*, *ACS Catal.* **11**, 5942–5950 (2021).
33. M. Peng *et al.*, *ACS Cent. Sci.* **7**, 262–273 (2021).
34. Z. Gao, A. Li, D. Ma, W. Zhou, *Top. Catal.* **65**, 1609–1619 (2022).
35. J. Miao, P. Ercius, S. J. L. Billinge, *Science* **353**, aaf2157 (2016).
36. Z. Li *et al.*, *Nat. Commun.* **14**, 2934 (2023).
37. Z. Liu *et al.*, *Science* **368**, 513–517 (2020).
38. S. Yao *et al.*, *Science* **357**, 389–393 (2017).
39. Z. Liu *et al.*, *Phys. Chem. Chem. Phys.* **18**, 16621–16628 (2016).
40. K. I. Hadjiivanov *et al.*, *Chem. Rev.* **121**, 1286–1424 (2021).
41. V. Muravev *et al.*, *Science* **380**, 1174–1179 (2023).
42. X. Q. Tang *et al.*, *Spectrochim. Acta A Mol. Biomol. Spectrosc.* **175**, 11–16 (2017).
43. S. Hanukovich, A. Dang, P. Christopher, *ACS Catal.* **9**, 3537–3550 (2019).
44. T. Hou, S. Zhang, Y. Chen, D. Wang, W. Cai, *Renew. Sustain. Energy Rev.* **44**, 132–148 (2015).
45. National Bureau of Statistics China (NBS China), The Profit of Industrial Enterprises above Designated Size in 2023 (NBS China, 2024); https://www.stats.gov.cn/english/PressRelease/202402/t20240201_1947130.html.

SUPPLEMENTARY MATERIALS

science.org/doi/10.1126/science.adt0682
Materials and Methods
Figs. S1 to S39
Tables S1 to S13
References (46–89)
Movies S1 to S4

Submitted 10 September 2024; accepted 14 January 2025
10.1126/science.adt0682